

**Shining Light on Dark Matter,
One Photon at a Time**

by

Brandon Leigh Allen

Submitted to the Department of Physics
in partial fulfillment of the requirements for the degree of

Doctorate of Science in Physics

at the

MASSACHUSETTS INSTITUTE OF TECHNOLOGY

June 2019

© Massachusetts Institute of Technology 2019. All rights reserved.

Author
Department of Physics
May 18, 2019

Certified by
Christoph E.M. Paus
Professor
Thesis Supervisor

Accepted by
Nergis Mavalvala
Associate Department Head for Education

**Shining Light on Dark Matter,
One Photon at a Time**

by

Brandon Leigh Allen

Submitted to the Department of Physics
on May 18, 2019, in partial fulfillment of the
requirements for the degree of
Doctorate of Science in Physics

Abstract

A search is conducted for new physics in final states containing a photon and missing transverse momentum in proton-proton collisions at $\sqrt{s} = 13$ TeV. The data collected by the CMS experiment at the CERN LHC correspond to an integrated luminosity of 35.9 inverse femtobarns. No deviations from the predictions of the standard model are observed. The results are interpreted in the context of dark matter production and limits on new physics parameters are calculated at 95% confidence level. For the two simplified dark matter production models considered, the observed (expected) lower limits on the mediator masses are both 950 (1150) GeV for 1 GeV dark matter mass.

Thesis Supervisor: Christoph E.M. Paus

Title: Professor

Acknowledgments

This is the acknowledgements section. You should replace this with your own acknowledgements.

Contents

1	The Large Hadron Collider	9
1.1	Experimental Apparatus	9
1.2	Collider Phenomenology	12
1.2.1	Parton Distribution Functions	13
1.2.2	Hard Scattering	14
1.2.3	Parton Shower	14
1.2.4	Hadronization	15
2	The CMS Detector	17
2.1	Inner Tracker System	19
2.2	Electromagnetic Calorimeter	21
2.3	Hadronic Calorimeter	23
2.4	Muon Chambers	23
2.5	Online Trigger System	23
2.6	Detector Simulation	24

Chapter 1

The Large Hadron Collider

1.1 Experimental Apparatus

The Large Hadron Collider (LHC) is a circular proton-proton collider, 27 km in circumference and between 40 and 175 m below the surface, located at the European Organization for Nuclear Research (CERN) on the French-Swiss border near the city of Geneva. Designed to collide protons at a maximum center-of-mass energy $\sqrt{s} = 14 \text{ TeV}$, the LHC has delivered collisions at $\sqrt{s} = 7, 8 \text{ TeV}$ during Run 1 (2010-2012) and at $\sqrt{s} = 13 \text{ TeV}$ during Run 2 (2015-2018). While the LHC is primarily a proton-proton collider, lead (Pb) ion beams of energy of up to 2.8 TeV per nucleon are used to produce lead-lead and proton-lead collisions. In this thesis, we focus exclusively on data recorded from proton-proton collisions during Run 2.

The LHC is the final stage of the CERN accelerator complex depicted in Figure 1-1. Hydrogen atoms are stripped of their electrons and accelerated to an energy of 50 GeV by the LINAC2 linear acceleration. Following this, they are injected into the Booster ring, the Proton Synchrotron (PS), and the Super Proton Synchrotron (SPS) and accelerated to 1.4, 26, and 450 GeV, respectively. After the SPS, the protons are injected into the two counter-circulating rings of the LHC in up to 2808 discrete bunches with a bunch spacing of 25 ns. The two beams intersect in eight places along the LHC with detector experiments CMS, ATLAS, LHCb, and ALICE each located at an intersection point.

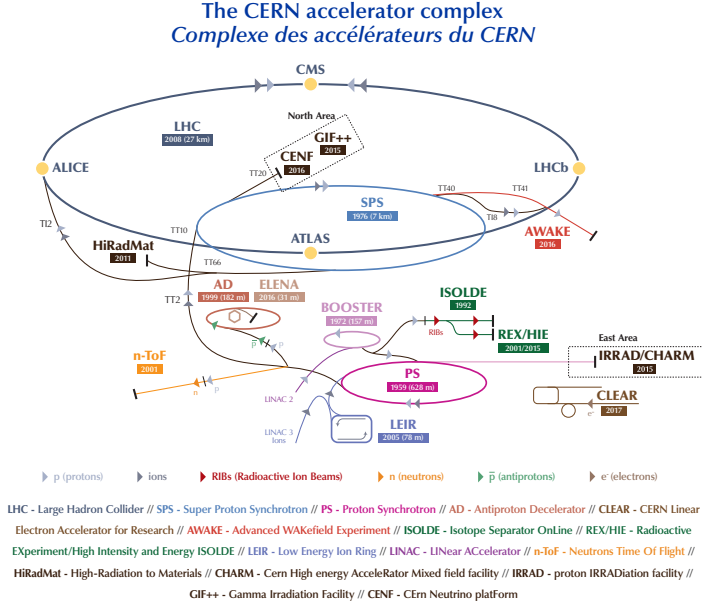


Figure 1-1: A schematic representation of the CERN accelerator complex. The LHC (dark blue) is fed protons by a chain of intermediate accelerators, beginning with LINAC2 (light pink). Reprinted from the CERN Document Server [1].

The LHC is a synchrotron containing 1232 superconducting NbTi dipole magnets measuring 15 m in length, each with a peak dipole field of 8.33 Tesla. There are an additional 492 quadrupole magnets measuring 5-7 m in length which focus the beams in between the dipole magnets. Due to space limitations in the tunnels, the beam pipes are magnetically coupled and the magnets share the same superfluid liquid helium cryostatic system to achieve the 1.9K temperature required to achieve the desired magnetic field strength.

The number of events produced at the LHC is given by

$$N(pp \rightarrow X) = \int dt L(t) \sigma(pp \rightarrow X), \quad (1.1)$$

where σ is the cross section of the process and L is the instantaneous luminosity of the machine given by

$$L = \frac{N_b^2 n_b f_{\text{rev}} \gamma}{4\pi \epsilon \beta^*} \times F, \quad (1.2)$$

where N_b is the number of particles per bunch ($\mathcal{O}(10^{11})$), n_b is the number of bunches

per beam, f_{rev} is frequency of revolution, γ is the Lorentz factor of the beam, ϵ is transverse emittance of the beam, β^* is beta function of the beam at the collision point, and F is the geometric luminosity reduction factor due to the crossing angle at the interaction point. The instantaneous luminosity decreases exponentially as a function of time due to N_b and n_b being reduced by collisions. The LHC is designed to deliver an initial instantaneous luminosity of $\mathcal{O}(10^{34}) \text{ cm}^{-2} \text{ s}^{-1}$.

As all known cross sections are time-independent, the total number of events is directly proportional to the integrated luminosity given by

$$L_{\text{int}} = \int_0^T dt L(t) = L(0)\tau_L (1 - e^{-T/\tau_L}), \quad (1.3)$$

where T is the time since starting collisions, $L(0)$ is the initial instantaneous luminosity, and $\tau_L \approx 15$ the characteristic beam loss timescale for the LHC. The total luminosity delivered by the LHC and recorded by CMS during the 2016 is shown in Figure 1-2.

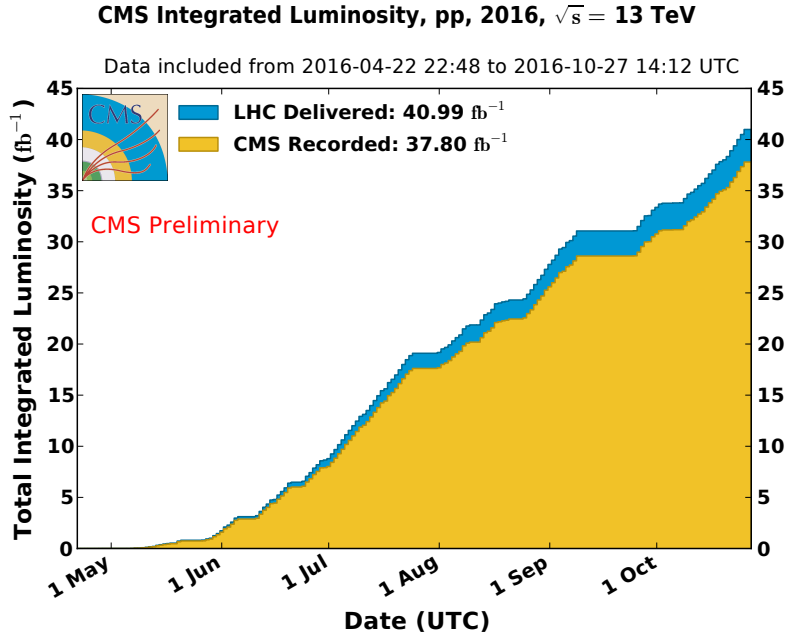


Figure 1-2: The total integrated luminosity of the LHC during proton-proton collisions during 2016.[] While a total luminosity of 41 fb^{-1} was collected, only a subset during which the detector operated optimally is used in this thesis. This corresponds to 36 fb^{-1} of data.

1.2 Collider Phenomenology

The proton is a composite particle consisting of valence quarks, sea quarks, and gluons, collectively referred to as partons. When colliding protons at the LHC, we are actually interested in the inelastic scattering of a pair of partons from the incident protons. Each parton a, b carries a fraction of the momentum of the incoming proton $x_{a,b}$ following the particle-dependent parton distribution functions (PDFs) $f_{a,b}$. The differential cross section for $2 \rightarrow N$ parton scattering process is given by

$$d\sigma(ab \rightarrow \{c_i\}) = \frac{(2\pi)^4}{2s} \left(\prod_i \frac{d^3 p_i}{(2\pi)^3} \right) \cdot \delta^4 \left(k_a + k_b - \sum_i p_i \right) \cdot |\mathcal{M}(ab \rightarrow \{c_i\})|^2 \quad (1.4)$$

where $k_{a,b} = x_{a,b}\sqrt{s}$ are the momenta of the incoming partons, $\{p_i\}$ are the momenta of the outgoing partons $\{c_i\}$, and \mathcal{M} is the matrix element of the process.

This parton level scattering, called the hard scattering process, is perturbatively calculable through standard QFT methods. However, the hard scattering does not include any effects related to the PDFs of the incoming partons or the decay and hadronization of the outgoing partons into the final state particles (called the parton shower), both of which involve non-perturbative aspects of QCD. Fortunately, the collinear factorization theorem states that the probability of obtaining the final state $X(\Theta)$ from a hadron collision can be calculated as the product of the probability that specific partons a, b are involved in the interaction, the probability for the hard scattering to produce outgoing partons $\{c_i\}$, and the formation of final state hadrons from these outgoing partons. The factorization process is not unique and requires the choice of an arbitrary energy scale μ_F , which defines a lower bound for interactions to be considered part of the hard scattering.

Including the effects from PDFs and parton showering (PS), the general cross section for $pp \rightarrow X(\Theta)$ is

$$\begin{aligned} \frac{d\sigma}{d\Theta}(pp \rightarrow X(\Theta)) &= \sum_{a,b} \int dx_a f_a(x_a, \mu_F) \cdot dx_b f_b(x_b, \mu_F) \\ &\quad \times d\sigma(ab \rightarrow \{c_i\}) \times D(\{c_i\} \rightarrow X(\Theta)) \end{aligned} \quad (1.5)$$

where the sum is over the initial state partons and D is the fragmentation function that describes parton shower process resulting in the observed final state. The following sections discuss the simulation of the three main elements of Equation 1.5: the parton distribution functions f_a , the hard scattering cross section $d\sigma$, and the parton shower and hadronization processes that contribute to the fragmentation function D .

1.2.1 Parton Distribution Functions

Due to soft collinear emissions from the partons, the behavior of the parton distribution functions depends on the factorization scale. Denoting the gluon PDF as $g(x, \mu_F)$ and the PDF for quark flavor i as $q_i(x, \mu_F)$, the analytic behavior of the PDFs is given by the DGLAP evolution equations

$$\mu_F \frac{d}{d\mu_F} \begin{pmatrix} q_i(x, \mu_F) \\ g(x, \mu_F) \end{pmatrix} = \frac{\alpha_s}{2\pi} \int_x^1 \frac{dy}{y} \begin{pmatrix} P_{qq}(x/y) & P_{qg}(x/y) \\ P_{gq}(x/y) & P_{gg}(x/y) \end{pmatrix} \begin{pmatrix} q_i(y, \mu_F) \\ g(y, \mu_F) \end{pmatrix} \quad (1.6)$$

where y is the fraction of momentum carried by initial parton and the P matrix elements are the splitting kernels defined by

$$\left. \begin{array}{l} P_{qq}(z) = \frac{4}{3} \left(\frac{1+z^2}{1-z} \right) \\ P_{qg}(z) = \frac{4}{3} \left(\frac{1+(1-z)^2}{z} \right) \\ P_{gq}(z) = \frac{1}{2} (z^2 + (1+z)^2) \\ P_{gg}(z) = 6 \left(\frac{1-z}{z} + \frac{z}{1-z} + z(1-z) \right). \end{array} \right| \quad (1.7)$$

The DGLAP equations cannot be solved analytically at a fixed scale. Instead, parameterized functional forms are fitted to data from many experiments. The results presented in this thesis use the NNPDF3.0 PDF set provided by the NNPDF collaboration. Figure 1-3 shows the quark and gluon PDFs for the proton. As $x \rightarrow 0$, the gluon fraction dominates while as $x \rightarrow 1$, the up-quark fraction $u(x, \mu_F)$ approaches $\frac{2}{3}$, the down-quark fraction $d(x, \mu_F)$ approaches $\frac{1}{3}$, and the gluon and sea quark fractions approach zero.

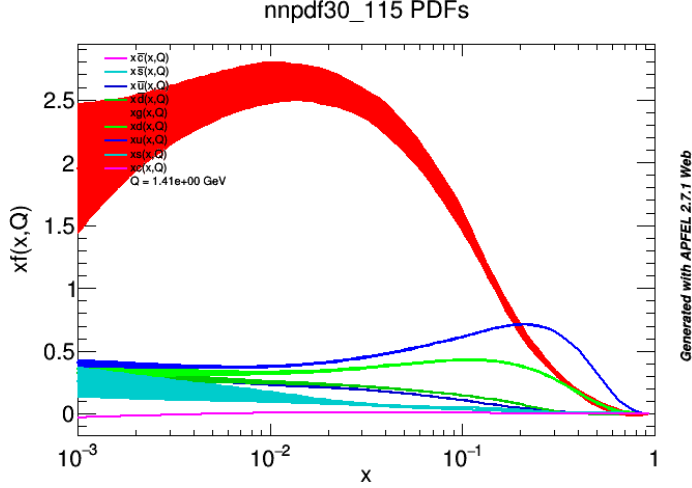


Figure 1-3: The various quark and gluon PDFs for the proton, as a function of momentum fraction x . The specific PDF set is the NNPDF3.0 118 NLO PDF set.

1.2.2 Hard Scattering

The hard scattering process is simulated using Monte Carlo generators that sample events with probability proportional to the phase space and matrix element. For the results contained in this thesis, the primary hard interaction is simulated using the MADGRAPH5 aMC@NLO generator, which can simulate to leading order (LO) in EW vertices and up to next-to-leading order (NLO) in QCD vertices.

1.2.3 Parton Shower

The parton shower is a sequence of splittings where one outgoing parton c_i emits a second soft and/or collinear particle j . Each splitting has an associated splitting kernel $P_{c_i \rightarrow c_{ij}}(z)$, where z is the momentum fraction carried by the initial parton. The allowed QCD splittings are $q \rightarrow qg$, $g \rightarrow q\bar{q}$, and $g \rightarrow gg$ and the allowed QED splittings are $f \rightarrow f\gamma$ and $\gamma \rightarrow f\bar{f}$. The kernels associated with these splittings are

$$\left| \begin{array}{l} P_{q \rightarrow qg}(z) = \frac{4}{3} \left(\frac{1+z^2}{1-z} \right) \\ P_{g \rightarrow q\bar{q}}(z) = \frac{1}{2} (z^2 + (1-z)^2) \\ P_{g \rightarrow gg}(z) = 3 \left(\frac{(1-z)(1-z)^2}{z(1-z)} \right) \\ P_{f \rightarrow f\gamma}(z) = Q_f^2 \left(\frac{1+z^2}{1-z} \right) \\ P_{\gamma \rightarrow f\bar{f}}(z) = N_C Q_f^2 (z^2 + (1-z)^2) \end{array} \right. \quad (1.8)$$

where Q_f is the charge of the fermion and N_C is the number of color states the fermion can occupy (3 for quarks and 1 for leptons). The cross section of a splitting is given by

$$\frac{d\sigma(ab \rightarrow \{c_i\}j)}{d\sigma(ab \rightarrow \{c_i\})} = P_{c_i \rightarrow c_ij}(z) \cdot \frac{\alpha_s}{2\pi} \cdot \frac{d\theta}{\theta} \cdot dz \quad (1.9)$$

where θ is the opening angle between c_i and j . These cross sections diverge as $\theta \rightarrow 0$ and $z \rightarrow 1$, meaning bare quarks producing many soft and collinear gluons. Then, these gluons further split to gg and $q\bar{q}$ pairs, which in turn emit even more soft and collinear gluons and photons. This process continues until the energy of the outgoing partons reaches Λ_{QCD} at which point hadronization occurs.

1.2.4 Hadronization

The QCD potential between two quarks can be approximated as $V(\vec{r}) \approx \kappa r$, where κ has been measured to be approximately 1 GeV/fm. The linear behavior of the potential is due to the attractive interactions between the gluons mediating the quark-quark interaction which confine the color field between the quarks into a tube 1 fm in diameter. As the quarks separate, the energy contained in this gluon tube increases linearly until it exceeds the mass of a $q\bar{q}$ pair. At this point, a new $q\bar{q}$ pair pops into existence through a quantum mechanical tunneling process, splitting the tube in two. Due to the difference in quark masses, only up, down, and strange quarks are produced, in a 10:10:3 ratio. This process continues until the energy of all the quarks have low enough energy to combine into stable hadrons.

The above procedure is a qualitative description of the Lund string model used. The Pythia event generator models hadronization using the Lund string model as well as the parton shower effects described in the previous section. All results in this thesis use the Pythia 8.2 program to simulate the parton shower and hadronization processes.

Chapter 2

The CMS Detector

The Compact Muon Solenoid (CMS) detector is one of two hermetic, general purpose detectors at the Large Hadron Collider. The original motivation for the experiment was the discovery of the Higgs boson by observing its decays to photons, electrons, and muons. Towards this end, the detector was built to fulfill the following goals:

- Unambiguous charge identification of muons with momenta up to 1 TeV
- 1 GeV mass resolution on 100 GeV pairs of muons, electrons, and photons
- Efficient triggering and tagging of τ lepton and b quark decays
- Good resolution on the hadronic energy and missing transverse energy
- Sufficient time resolution to deal with 40 MHz of collisions

The CMS detector consists of four main subdetectors: the inner tracker system, the electromagnetic calorimeter (ECAL), the hadronic calorimeter (HCAL), and the muon chambers. The first three are within the field volume of the eponymous 3.8 T superconducting NbTi solenoid magnet while the muon chambers are embedded in the return yoke of the magnet. Additionally, there is an online triggering system to reduce readout from 40 MHz to $\mathcal{O}(1)$ kHz for prompt reconstruction.

The overall layout of the CMS detector is shown in Figure 2-1. The CMS detector has a weight of 12500 tons, a length of 22 m, a diameter of 15 m, and a cylindrical

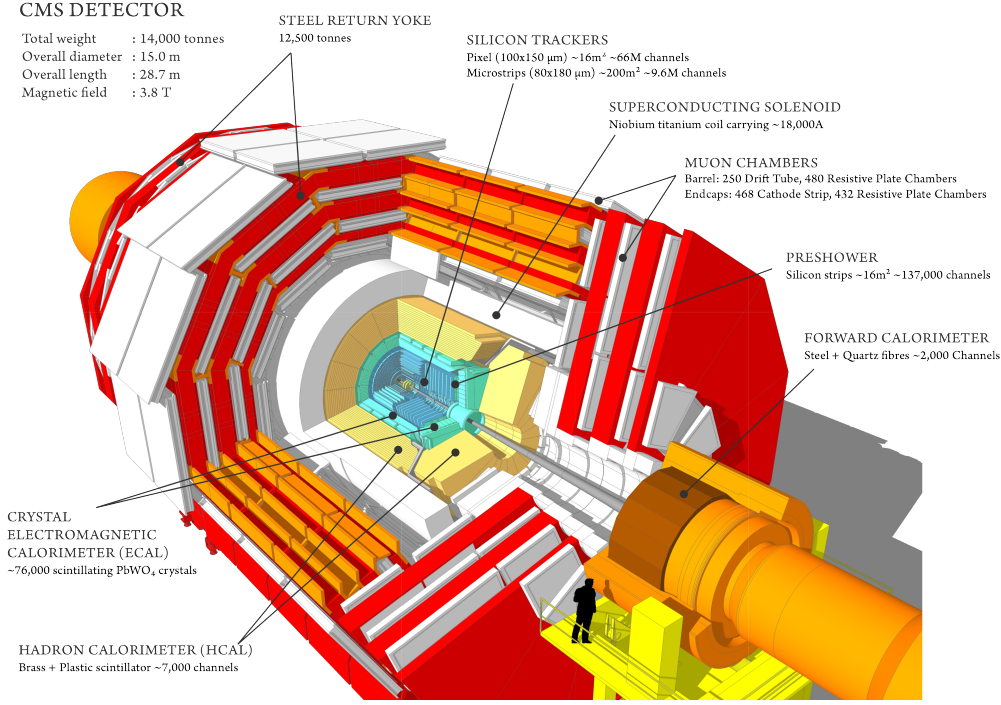


Figure 2-1: A cutaway view of the CMS detector. The labels identify the solenoid as well as the different subdetectors and their components. Reprinted from Reference [1].

geometry with concentric barrel shaped detectors in the central region and disc shaped detectors in the forward region. The following coordinate system is used when working with the CMS detector:

- distance z along the beam axis
 - $z = 0$ at the center of the detector
 - positive corresponds to counter-clockwise as seen from the sky
- distance r from the beam axis
- polar angle θ measured with respects to the positive z -axis
- azimuthal angle ϕ in the plane orthogonal to the beam axis

In addition to these four main coordinates, we define the right-handed cartesian x and y coordinates perpendicular to the beam axis, with the positive x -axis pointing

from the center of the detector to the center of the LHC ring and the positive y -axis pointing upwards.

The four-momentum of a particle is $p = (p_x, p_y, p_z, E)$ in the cartesian basis and a particle of mass m produced at rest in the center of the detector has $p = (0, 0, 0, m)$. While the momenta along the beam axis of the two incoming protons are equal, the momenta of the incoming partons involved in the hard scattering often are not as discussed in Section 1.2. Thus, we define two kinematic quantities that are Lorentz-invariant with respect to a boost along the beam axis: the transverse momentum $\vec{p}_T = p_x \hat{x} + p_y \hat{y}$ with magnitude $p_T = \sqrt{p_x^2 + p_y^2}$ and the pseudorapidity $\eta = -\ln \tan \theta/2$.

In terms of p_T , η , and ϕ , we have the following expressions for our cartesian variables: $p_x = p_T \cos \phi$, $p_y = p_T \sin \phi$, $p_z = p_T \sinh \eta$, and $E = p_T \cosh \eta$, with the last equality assuming the mass of the particle is negligible compared to its momentum. In terms of our Lorentz-invariant coordinates, the four-momentum of a given particle is $p = (p_T, \eta, \phi, E)$. Additionally, the spatial separation of two particles is given by $\Delta R = \sqrt{(\Delta\phi)^2 + (\Delta\eta)^2}$ and the fiducial acceptance of the CMS detector is from $0 \leq \phi < 2\pi$ and $-5 \leq \eta \leq 5$.

2.1 Inner Tracker System

Closest to the interaction point, the inner tracker system identifies charged particles and measures their momenta. Additionally, high resolution tracks are used to identify primary and secondary vertices. The magnetic field in the tracker volume is uniform with strength 3.8 T and field lines parallel to the beam direction. The tracker volume extends to 1.2 m in r and 2.9 m in z , providing coverage for $|\eta| < 2.5$, and is instrumented with silicon pixels and strips. Each silicon sensor is a p - n semiconductor junction with a bias voltage applied. When a charged particle passes through the depletion region of the junction, electron-hole pairs are produced and collected by the readout electronics. A schematic of the inner tracker system is shown in Figure 2-2.

The 66 million individual pixel sensors, each measuring $285 \mu\text{m} \times 100 \mu\text{m} \times 150 \mu\text{m}$ in $r \times r\phi \times z$, are arranged into seven layers: three cylindrical barrels at $r =$

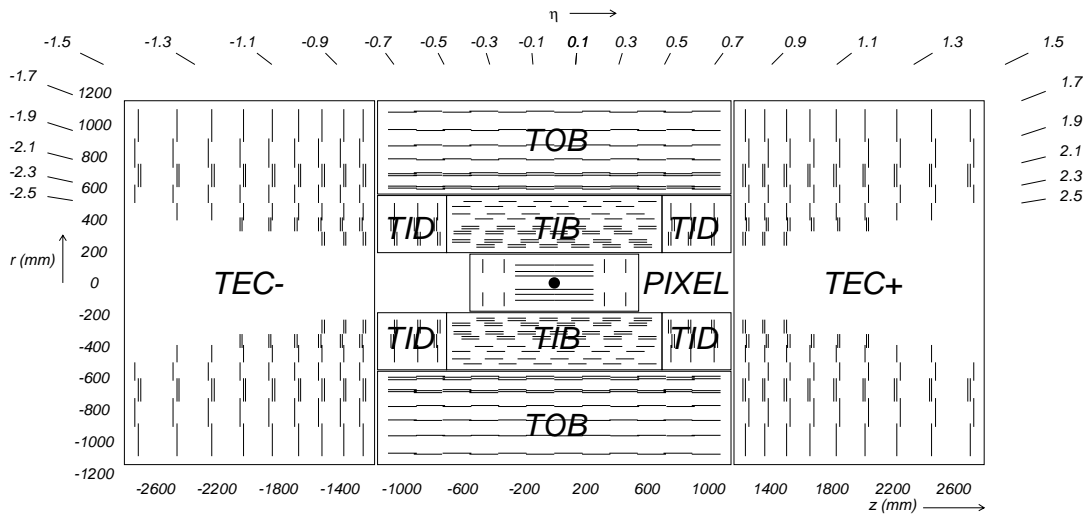


Figure 2-2: A schematic view of the CMS inner tracker system. Silicon pixel and strip detectors are shown. The volumes labeled TIB, TID, TOB, and TEC are all strip trackers. The double lines indicate back-to-back modules that deliver stereo hits. Reprinted from Reference [1].

4.4, 7.3, 10.2 cm and two bi-layer endcap annuli at $z = \pm 34.5, \pm 46.5$ cm. Due to the geometry of the pixel detector, tracks typically cross the sensor at a 20° angle, leading to the charge deposit from a single track to be shared among multiple pixels in the same layer. The exact position of a particle in each layer is determined by interpolating the signals from multiple adjacent pixels with an analog pulse height greater than a tuneable read-out threshold. Thus, each pixel hit is localized to an area of $\sim 15\text{ }\mu\text{m} \times 20\text{ }\mu\text{m}$ in $r\phi \times z$, providing a much higher spacial resolution than the raw pixel spacing.

The pixels are surrounded 9.3 million silicon strips measuring $10\text{ cm} \times 80\text{ }\mu\text{m}$ arranged in ten cylindrical layers in the barrel and twelve disks in each endcap. The Tracker Inner Barrel (TIB) consists of the first four layers and extends from 20 cm to 55 cm in the radial direction while out six layers constitute the Tracker Outer Barrel (TOB) with an outer radius of 116 cm and extent in $|z|$ of 118 cm. The remaining area in the barrel is covered by the Tracker Inner Disk (TID), consisting of the three disks located from 80 to 90 cm in $|z|$. The Tracker EndCaps (TEC) have nine disks each and cover the region $124\text{ cm} < |z| < 282\text{ cm}$.

The majority of the strips are oriented perpendicular to the ϕ direction: parallel to the beam pipe in the barrel region and radially aligned in the endcap region. The strip pitch varies from 80 to 184 μm with the smallest pitch in the innermost layer. This detector geometry provides good resolution in the r - ϕ plane for barrel and the z - ϕ plane for the endcap but little information on the orthogonal directions. To compensate for this, one third of the strips are double-layered with a stereo angle of 100 mrad between the layers. Matching hits between adjacent layers enables a measurement of the z and r coordinates in the barrel and endcap, respectively. The final spacial resolution is 10-50 μm in the direction perpendicular to the strips and 100-530 μm in the parallel direction on the stereo modules.

2.2 Electromagnetic Calorimeter

The electromagnetic calorimeter (ECAL) is a homogeneous, hermetic calorimeter composed of 76,000 lead tungstate (PbWO_4) crystals. High density (8.3 g/cm³) lead tungstate was chosen due to its radiation hardness, fast scintillation decay time constant of 25 ns, small Moliere radius $r_M = 21.9$ mm, and short radiation length $X_0 = 8.9$ mm. All of these factors combine to enable the construction of a compact calorimeter with high granularity and excellent energy resolution.

Figure 2-3 shows the layout of the ECAL. The central barrel region (EB) has 61200 crystals arranged in a 170×360 η - ϕ grid (0.0174 \times 0.0174 granularity) with a coverage up to $|\eta| = 1.44$ while the two endcap annuli (EE) each have 7324 crystals organized in a x - y grid with coverage in the range $1.479 < |\eta| < 3.0$. Each crystal in the EB has a truncated pyramidal shape with a length of 230 mm, a 22 mm \times 22 mm front-face cross-section, and a 26 mm \times 26 mm rear-face cross-section while a crystal in the EE has a cuboid-like shape with a length of 220 mm, a 28.6 mm \times 28.6 mm front-face cross-section, and a 30 mm \times 30 mm rear-face cross-section. The cross-sectional area of approximately one Moliere radius and length of approximately 25 radiation lengths allows just a few crystals to contain the entire transverse and longitudinal development of the shower. To reduce the likelihood of the primary photon or electron

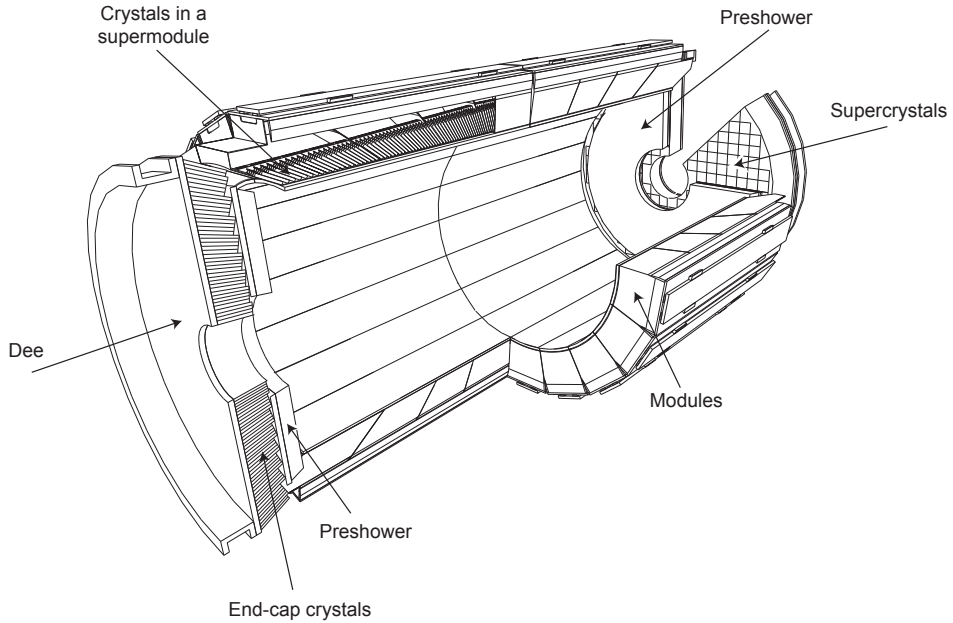


Figure 2-3: The layout of the CMS electromagnetic calorimeter. The barrel and endcap calorimeters are shown. The pre-shower detector sits in front of the endcaps. Reprinted from Reference [1].

emerging from the hard scattering depositing most of its energy in passive material, the crystals do not point directly to the interaction region.

The interactions between the 3.8 T magnetic field and the geometries of the ECAL lead to the selection of different photosensors in the barrel and endcaps. In the endcaps, the magnetic field is parallel to the path of the photoelectrons and has a negligible effect on the gain, while in the barrel, the magnetic field is perpendicular and reduces the gain by a factor proportional to the distance traveled by the photoelectrons. Thus, in the barrel, solid-state reverse-structure avalanche photodiodes (APDs) with a depletion layer of $6.0 \pm 0.5 \mu\text{m}$ are used, while photomultiplier tubes with a single gain stage and a very fine copper mesh anode called vacuum phototriodes (VPTs) are used in the endcaps. Two APDs with an active area of 25 mm^2 are glued to the rear of each crystal in the barrel while only one VPT with an active area of 280 mm^2 is needed per crystal in the endcap. The APDs and VPTs amplify the initial signal of approximately 4.5 photoelectrons per MeV of energy deposit per

crystal by a factor of 50 and 10, respectively.

The small signals from the photodetectors are shaped and amplified in the Multi-Gain Preamplifier (MGPA) and a 12-bit analog-to-digital converter (ADC) samples the pulse every 25 ns. Each output voltage pulse has a length of approximately 300 ns, with the maximum at approximately 75 ns and a slow decay afterwards. The MGPA has multiple gain modes of 12, 6, and 1, and the gain chosen for the output decreases once the signal has saturated the previous gain setting. After the pulse falls below the saturation threshold, the lower gain setting is maintained for the next five samples. This mechanism provides a dynamic signal range from a few MeV to a maximum of 1.5 TeV in the barrel and 3.1 TeV in the endcaps.

The energy resolution of the ECAL was measured using an electron beam to be

$$\frac{\sigma_E}{E} = \frac{2.8\%}{\sqrt{E/\text{GeV}}} \oplus \frac{12\%}{E/\text{GeV}} \oplus 0.3\%, \quad (2.1)$$

where E is the energy of the incident particle and the three terms on the RHS are the stochastic, noise, and constant terms, respectively. The stochastic term is dominated by event-to-event fluctuations in the lateral shower containment and a photo-statistics contribution of 2.1%. Electronic and digitization noise drive the noise term while the constant term comes from a non-uniform longitudinal light collection and intercalibration errors.

2.3 Hadronic Calorimeter

Our big brassy boi.

2.4 Muon Chambers

The red ones.

2.5 Online Trigger System

How we choose events.

2.6 Detector Simulation

Gotta get predictions somehow.